Structural and thermoelectric properties of $FeSb_3$ skutterudite thin films

M. V. Daniel,[1,*] L. Hammerschmidt,[2] C. Schmidt,[1] F. Timmermann,[1,†] J. Franke,[1] N. Jöhrmann,[1] M. Hietschold,[1] D. C. Johnson,[3] B. Paulus,[2] and M. Albrecht[1,†]

[1]*Institute of Physics, Technische Universität Chemnitz, 09107 Chemnitz, Germany*

[2]*Institute of Chemistry and Biochemistry, Freie Universität Berlin, 14195 Berlin, Germany*

[3]*Chemistry Department, University of Oregon, 1253 University of Oregon, Eugene, Oregon 97403, USA*

(Received 11 December 2014; revised manuscript received 15 January 2015; published 12 February 2015)

Skutterudites are promising materials for future thermoelectric applications. Whereas the skutterudite $CoSb_3$ is intensively studied, very few investigations for $FeSb_3$ are performed due to its metastable character and the comparably low decomposition temperature. In this work, single-phase $FeSb_3$ thin films were prepared by codeposition of Fe and Sb using molecular beam epitaxy at room temperature followed by postannealing. The transport properties of a Fe-Sb composition series were determined and reveal high power factors $S^2\sigma$ up to 14 $\mu W/K^2cm$. Furthermore, the structural parameters, the electronic structure, and the transport parameters were calculated by density functional theory, giving excellent agreement with the experimental data.

DOI: 10.1103/PhysRevB.91.085410 PACS number(s): 68.55.−a, 73.50.Lw, 71.15.Mb

I. INTRODUCTION

Since energy efficiency is becoming more and more important and novel nanostructured materials as well as new thermoelectric material groups have recently been introduced, the field of thermoelectricity is in the focus of current research activities. Slack [1] has provided a guideline for finding novel thermoelectric materials. Complex unit cells in combination with large atomic masses and low electronegativity differences of the individual atoms, as well as large carrier mobilities, are needed for high efficiencies [1,2]. This has resulted finally in the framework of "phonon glass-electron crystal" (PGEC) materials [1]. The electric properties of these materials should have a metal-like behavior, while the thermal properties should show characteristics of a glass, thus fulfilling the requirement of a thermoelectric material with a large Seebeck coefficient S, a high electric conductivity σ, and a low thermal conductivity κ.

The PGEC approach is nicely represented, for instance, in skutterudites [2]. The most promising skutterudite being investigated at the moment is $CoSb_3$ [2,3]. Another representative of this material group is $FeSb_3$. Compared to $CoSb_3$, a softening of the phonon modes was observed, which indicated a lower speed of sound in $FeSb_3$ and thus a lower lattice thermal conductivity [4]. However, the $FeSb_3$ phase is not an equilibrium phase. Since this compound is metastable, a special way of preparation far from equilibrium is needed. The only successful approach reported in the literature so far is based on the modulated elemental reactant method (MERM) [5,6]. Hence only a few publications exist and are mainly limited to the structural characterization of $FeSb_3$ thin films [4–6], while a detailed thermoelectric characterization is missing. For the MERM approach, the elements Fe and Sb were deposited layer by layer on nonheated substrates. The metastable nature of this phase limits the thin-film preparation to low temperatures combined with a postannealing step to achieve crystalline films. It is believed that the annealing process leads first to a homogeneous mixing of the multilayer structure by interdiffusion and later to its crystallization [5]. Single-phase skutterudite films are only obtained for films with a Sb excess compared to the stoichiometric value of 75 at. % of $FeSb_3$. However, due to the large amount of individual layers, the deposition process for the MERM method is rather complex.

In this work, it was shown that single-phase $FeSb_3$ films can also be achieved by codeposition at room temperature followed by a postannealing step. A Fe-Sb composition series was deposited at room temperature followed by postannealing at various temperatures. The annealed films were afterwards structurally and thermoelectrically characterized and the power factors were determined. Furthermore, the structural parameters, the electronic structure, and the transport properties were calculated using density functional theory (DFT), revealing excellent agreement with the experimental results.

II. EXPERIMENTAL AND COMPUTATIONAL DETAILS

A. Film preparation

Fe-Sb films with different Sb content between 70 and 80 at. % and a nominal thickness of 30 nm were prepared by molecular beam epitaxy (MBE) in ultrahigh vacuum (UHV) with a base pressure of 1×10^{-10} mbar. Both elements were thermally evaporated from an effusion cell and deposited in parallel on nonheated substrates using thermally oxidized silicon [SiO_2(100nm)/Si(100)] or special glass substrates (Ohara "S-TIH23" [7]). To achieve the desired stoichiometry, the Sb flux was kept constant at 0.7 Å/s and the Fe flux was varied. After deposition, a postannealing step was applied to obtain crystalline films. The films were therefore heated in UHV with a rate of 10 K/min up to the desired annealing temperature and kept at this temperature for one hour.

B. Structural characterization

The composition and the thickness of the as-deposited and annealed films was determined by Rutherford backscattering spectrometry (RBS). He^+ ions were accelerated by a Van

*marcus.daniel@physik.tu-chemnitz.de

†Present address: Institute of Physics, University of Augsburg, 86159 Augsburg, Germany.

de Graaff generator to 1.7 MeV and the used scatter angle was 170°. The backscattered ions were detected with a multichannel semiconducting detector. The collected total charge was typically 10 μC.

An as-deposited Fe-Sb film was further analyzed by differential scanning calorimetry (DSC) using a Netzsch DSC 200 system to determine the characteristic crystallization temperatures. The film was therefore lifted from the used polymethyl methacrylate (PMMA) substrate. The obtained film material was heated twice in a nitrogen atmosphere while measuring the DSC voltage. By subtracting the second curve from the first one, irreversible events can be extracted. Details of the measurement procedure are given elsewhere [8].

The phase formation in the films was investigated by x-ray diffraction (XRD) with a laboratory diffractometer with an implemented monochromator, which is measuring in Bragg-Brentano geometry using Cu K_α radiation. The contribution of the Cu $K_{\alpha 2}$ radiation was subsequently removed from the data by the Rachinger algorithm [9], thus the resulting XRD patterns correspond to the Cu $K_{\alpha 1}$ radiation with a wavelength of 1.5406 Å. To identify peaks and phases, a literature database [10] was used. Additionally, specific parameters of the crystal structure were extracted from the scans by performing Rietveld refinement with the software FULLPROF [11,12].

The surface morphology of the sample was imaged by atomic force microscopy (AFM). In this work, an AFM DI Dimension 3000 (Digital Instruments) was used in the constant force tapping mode.

The grain size was further determined by using electron backscatter diffraction (EBSD). The measurements were performed using a scanning electron microscope (SEM) of the type FEI Nova NanoSEM 200 equipped with a Nordlys II EBSD detector from HKL Technologies. An incident angle of 70 ° and an electron energy of 15 keV were used. The recorded data were postprocessed by using the software HKL CHANNEL5 from Oxford Instruments.

C. Transport measurements

Transport measurements at various temperatures were performed with homemade setups. The electric conductivity and the Hall coefficient were measured in van der Pauw geometry by using spring-loaded contacts. The Seebeck coefficient was measured based on the measurement setup introduced by Compans [13], where each side of the sample is in contact with a heatable Cu block. The sample is overspanning the slit in between both blocks, and by heating both sample sides differently, a temperature gradient can be applied to the sample and the corresponding thermovoltage can be determined. The film temperature of each sample side was measured by two Cu/Constantan thermocouples (low-temperature and room-temperature setup) or two Ni/NiCr thermocouples (high-temperature setup). The used measurement routine also follows the work of Compans. However, in contrast, no reference material was used and the thermovoltage was measured against the individual legs of the thermocouples. The low-temperature setup was calibrated by the measurement of a reference lead foil, whereas the measured data by using the room-temperature and the high-temperature setup were corrected by the known temperature dependences of the absolute Seebeck coefficients of the individual legs [14]. The high-temperature measurements were performed under high vacuum conditions ($<1 \times 10^{-6}$ mbar).

D. Computational details

Plane-wave density functional theory calculations were performed by applying the VASP 5.3.3 program package [15–18] together with the GW projector augmented wave (PAW) potentials [19–21]. In addition, local-density approximation (LDA) [22], Perdew-Burke-Ernzerhof (PBE) [23], and PW91 [24,25] functionals have been employed. Electronic wave functions were expanded to an energy cutoff of 350 eV. k-point grids were Γ centered and were constructed automatically via the Monkhorst-Pack scheme. An $8 \times 8 \times 8$ k-point mesh was applied for full structure relaxations, while the mesh was increased to values of $28 \times 28 \times 28$ for calculations of the electronic density of states and transport properties. Such a dense mesh is necessary to ensure converged electronic properties.

The full structure relaxation was performed by applying the RMM-DIIS quasi-Newton algorithm [26] together with a Gaussian smearing with a smearing factor of 0.001 eV and a force convergence criterion of 10^{-4} eV/Å^2. Further decreasing the smearing factor has no effect on the minimum structure. The electronic density of states was computed by applying the tetrahedron method with Blöchl corrections [27]. Sampling of band structures was performed along high-symmetry paths in the Brillouin zone.

DFT calculations were either performed spin polarized or unpolarized and the corresponding electronic structures are presented. Transport properties were obtained from the unpolarized ground state within the limits of Boltzmann theory [28–30] and the constant relaxation time approximation as implemented in the BOLTZTRAP code [31]. In short, BOLTZTRAP performs a Fourier expansion of the quantum chemical band energies. This allows one to obtain the electronic group velocity v and inverse mass tensor M^{-1}, as the first and second derivatives of the bands with respect to k. Applying v and M^{-1} to the semiclassical Boltzmann equations, the transport tensors can be evaluated, which reduce to scalar transport properties in an isotropic crystal such as $FeSb_3$.

III. RESULTS AND DISCUSSION

A. Fe-Sb thin-film composition series

1. Crystallization process

The DSC method was used to characterize the phase formation of a Fe-Sb film with a Sb content of 76 at. % in dependence of the heating temperature. The DSC difference curve was obtained in a nitrogen atmosphere and is shown in Fig. 1(a). To relate the occurring exothermic peaks to the corresponding phase formation, XRD ($\theta/2\theta$) scans were performed on similar samples annealed for 20 min at temperatures slightly below and above the transition temperatures found by DSC. The used parameter of the annealing process were chosen comparable to the DSC measurements (N_2 atmosphere, same heating/cooling rate). The corresponding XRD scans are shown in Fig. 1(b). The as-deposited film and the film

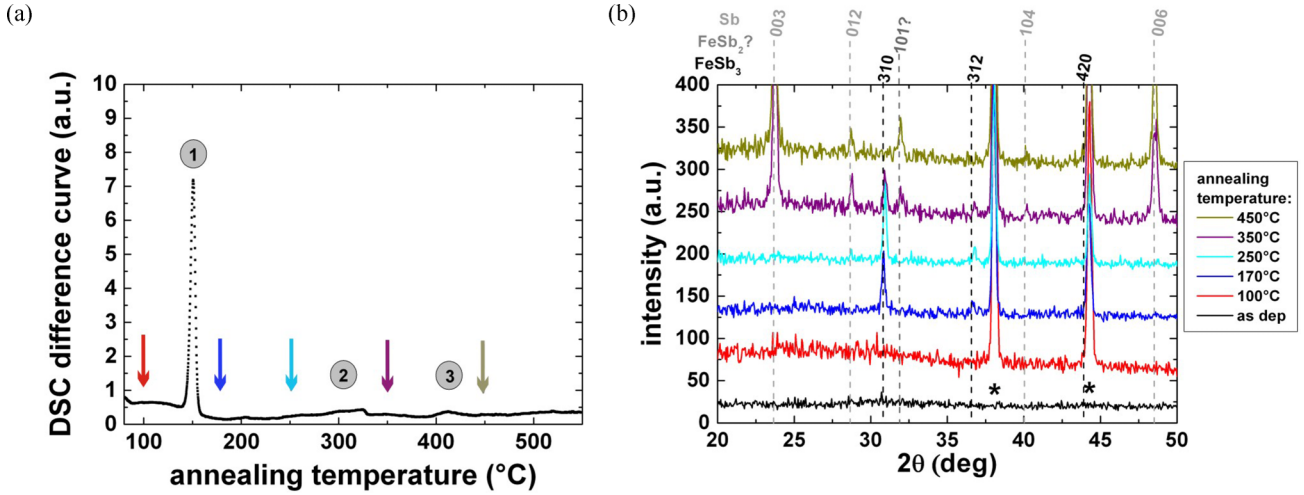

FIG. 1. (Color online) (a) DSC curve of a Fe-Sb film deposited at room temperature. The initial Sb content was 76 at. % Sb. The curve reveals three exothermic transition processes at 150.7, ∼300, and ∼400°C marked by the numbers. Similar samples were annealed at the temperatures indicated by the colored arrows, and the corresponding XRD ($\theta/2\theta$) scans of these samples are shown in (b) in the same color. Peaks originating from the sample holder (aluminum) are marked with an asterisk. They are not observed for the as-deposited film due to the larger size of this sample.

annealed at 100 °C are amorphous. Since the film annealed at 170 °C reveals only the skutterudite $FeSb_3$ phase, it could be demonstrated that the first peak appearing at 150.7 °C belongs to the crystallization temperature of this phase, which is in rough agreement with 140–150 °C given in the literature [5]. Two stronger and relatively broad peaks were found at about 300 and 400 °C. At about 300 °C, the skutterudite phase already starts to decompose and the formation of the Sb phase with a (001) texture is observed. The (001) peak is much more pronounced than the (012) peak of Sb, for which an intensity ratio ($I_{(001)} : I_{(012)}$) of 1:4 is expected for polycrystalline Sb due to its crystal structure and symmetry. Please note that the growth of textured Sb was only obtained for annealing in a nitrogen atmosphere and not for annealing in UHV. The peak appearing at $2\theta \sim 32°$ could not be identified and might correspond to the (101) reflection of $FeSb_2$. However, other reflections of this phase were not detected. For temperatures larger than 400 °C, only the Sb phase and the unknown phase (probably $FeSb_2$) can be detected by XRD. The $FeSb_3$ phase has completely vanished. The decomposition temperature is comparably low, since the phase is metastable and the energy needed to induce the decomposition into more stable phases is small. Thus it is necessary to keep the films below 300 °C, which is the maximum possible working temperature of the $FeSb_3$ films.

2. *Structural properties of* Fe-Sb *thin films*

Based on the results shown before, Fe-Sb films with a nominal thickness of 30 nm were codeposited on SiO_2 (100 nm)/Si(100) substrates at room temperature and afterwards annealed for one hour in UHV at the following annealing temperatures: 150, 200, 250, and 300 °C.

The phase formation of the codeposited films was investigated by XRD in dependence on the annealing temperature and on the Sb content of the films. The $FeSb_3$ skutterudite phase could only be found for a Sb content larger than 75 at. %, as summarized in Table I, which is in agreement with results found in the literature [5]. The obtained XRD ($\theta/2\theta$) scans for a film series with a Sb content of ∼77 at. % are exemplified in Fig. 2(a). While the initial films are amorphous, the skutterudite phase is already observed for films annealed at 150 °C. This is in agreement with the crystallization temperature of 150.7 °C found by DSC. For annealing temperatures of 150, 200, and 250 °C, single-phase skutterudite films were achieved in a Sb composition range between 76 and 80 at. % (see Table I). The upper limit, where additionally the Sb phase is formed, cannot be given, since no samples with larger Sb content than 80 at. % (or 79 at. % for 200 and 250 °C) were prepared for this study. For an annealing temperature of 300 °C, it was possible to get films with the skutterudite phase in the composition range between 76 and 77 at. %. For 76 at. %, single-phase films were achieved; for 77 at. %, indications for the formation of the Sb phase are additionally revealed. These results can also be seen in the corresponding XRD ($\theta/2\theta$) scan in Fig. 2(a).

With increasing annealing temperature, a peak shift towards higher angles and thus a decreasing lattice constant is observed. This effect becomes stronger for Sb-rich samples and can be attributed mainly to better crystallinity by less Sb interstitials and Sb evaporation, resulting in a relaxation towards the smaller equilibrium lattice constant of stoichiometic $FeSb_3$ films, as also observed for Sb-rich $CoSb_3$ films [8,32]. Thus this equilibrium lattice constant a (neglecting stress) can be determined from XRD measurements of single-phase $FeSb_3$ films with (nearly) stoichiometric Sb content after annealing at 300 °C. Therefore, a XRD ($\theta/2\theta$) scan of an annealed $FeSb_3$ film with a Sb content of 76 at. % was analyzed by performing a Rietveld refinement, shown in Fig. 2(b). The extracted values are summarized in Table II and compared with both results obtained by a full structure relaxation using plane-wave density functional theory calculations and values reported in the literature [4]. The experimentally determined lattice constant of 9.154 Å is in good agreement with the

TABLE I. Phase formation of annealed Fe-Sb films in dependence of the annealing temperature.

Annealing temp. (°C)	Sb content (at. %)					
	70–71	72–73	74–75	76–77	78–79	80–81
150		$FeSb_2$	$FeSb_2$		$FeSb_3$	$FeSb_3$
200		$FeSb_2$	$FeSb_3$, $FeSb_2$	$FeSb_3$	$FeSb_3$	
250	$FeSb_2$	$FeSb_2$,Sb	$FeSb_3$, $FeSb_2$	$FeSb_3$	$FeSb_3$	
300	$FeSb_2$	$FeSb_2$, Sb	$FeSb_3$, $FeSb_2$	$FeSb_3$	$FeSb_3$, Sb	

DFT calculations using the PBE and the PW91 functionals and it is also larger than the one of $CoSb_3$ (9.0057 Å [8]), as expected. Only the lattice constant obtained by LDA is quite underestimated. Indeed, LDA is known to generally underestimate lattice constants of solids [33,34]. PBE and PW91 tend to rather overestimate these values, e.g., in the $CoSb_3$ case [34], but generally show good agreement with experiments. Nevertheless, the obtained lattice constant is smaller than the reported one of 9.2383 Å [4]. These differences could occur due to the different deposition methods, different purity of the used elements, different composition, different substrates, or different annealing parameters. In the cited work [4], the films were deposited on a relatively thin Kapton foil, which might have an influence here. Furthermore, the annealing was performed under a nitrogen atmosphere at 137 °C and a poor crystallinity with higher defect density is expected for such a low annealing temperature (and in the case of comparable annealing times).

Furthermore, the independent atomic coordinates y and z of the Sb atoms can also be extracted from the refinement. Both coordinates are additional free parameters of the skutterudites lattice structure (space group $Im3$) and they are very important for the electronic band structure and thus for the corresponding thermoelectric properties [34]. By comparing the experimental and the theoretical data of both y and z, good agreement can also be found (see Table II), which is a prerequisite for performing the calculation of the electronic structure and the transport properties based on the calculated structural parameters.

Please note that the atomic coordinates calculated by using different functionals agree very nicely with each other. Furthermore, spin polarization has almost no effect on the two free Sb atomic positions y and z and only a small effect on the lattice constant (see Table II). For the PBE and the PW91 functionals, the lattice parameter deviates, for instance, by about 0.02 Å from the spin-polarized DFT results. Consequently, from a structural point of view, neglecting spin polarization is well justified.

The change of the surface morphology in dependence on the Sb content was investigated by AFM. Films annealed at temperatures below 250 °C are rather smooth and no noteworthy changes of the surface morphology were observed for different Sb content. Films annealed at 250 and 300 °C exhibit only a weak dependence on the Sb content and the root-mean-square roughness of these films is still below 1 nm. Single-phase $FeSb_3$ films reveal a smooth fine-grained structure, as shown in Figs. 3(a) and 3(b). Typical surface cracks were found in some cases for $FeSb_3$ films annealed at 300 °C [Fig. 3(b)]. The cracks occur at the grain boundaries due to the mismatch in lattice expansion coefficient of the substrate and film [35], which can be seen also in the EBSD band contrast map shown in Fig. 3(c). Band contrast maps reveal a bright contrast for positions, where a crystalline skutterudite structure is clearly observed, and a dark contrast for points, where no crystalline structure is detected (such as amorphous regions or grain boundaries). Each separated area corresponds to a grain with different orientation [35] and

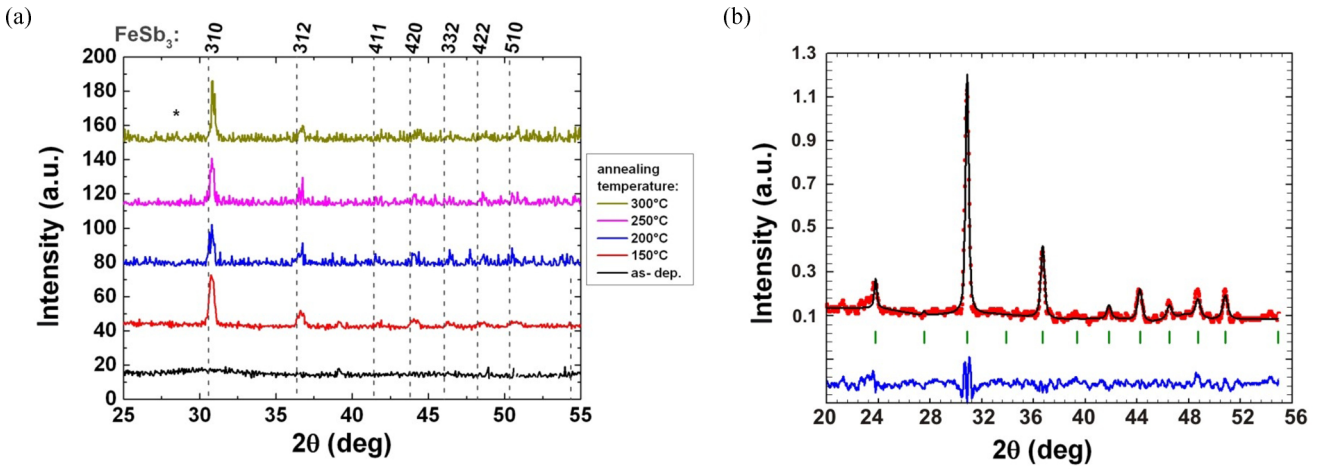

FIG. 2. (Color online) (a) XRD ($\theta/2\theta$) scans of a Fe-Sb film series with a Sb content of 77 at. % in dependence of the annealing temperatures. Only reflections of the skutterudite phase can be seen and a small peak shift towards higher angles is observed with increasing annealing temperature. The asterisk marks the position of the Sb (012) peak. (b) A Rietveld refinement was performed for a XRD scan of Fe-Sb film with 76 at. % Sb annealed at 300 °C.

TABLE II. Experimentally and theoretically obtained lattice constants a and independent Sb atomic coordinates y and z. The experimental values of this work were extracted by Rietveld refinement from a XRD ($\theta/2\Theta$) scan of a Fe-Sb film with a Sb content of 76 at. %, which was annealed at 300 °C. The DFT calculations were performed with different functionals (LDA, PBE, and PW91). The results of spin-polarized calculations are given in parentheses.

	a / Å	y	z
Expt. (300 K)	9.154	0.334	0.158
Expt. (300 K) [4]	9.2384	0.3399	0.1573
LDA calc.	8.947 (8.943)	0.337 (0.337)	0.161 (0.161)
PBE calc.	9.151 (9.167)	0.337 (0.341)	0.160 (0.160)
PW91 calc.	9.153 (9.174)	0.337 (0.341)	0.160 (0.160)

the grain boundaries exhibit a thickness smaller than 50 nm. The average grain size can be extracted by measuring the size of several grains in the image. As a result of drifts in the vertical direction during the EBSD measurement, which was proven by recording a SEM picture before and after the EBSD measurement, only the horizontal grain size can be analyzed accurately. A mean grain size of 1.3 μm could be extracted from these images. This value is in the same range as the grain size found for annealed $CoSb_3$ thin films [8].

To conclude, it was demonstrated that single-phase $FeSb_3$ films can be prepared by codeposition using MBE technique. This implies that eventually occurring preordering processes during the codeposition (which are excluded by using the MERM method) do not result in nucleation sites for the more stable phases such as $FeSb_2$. Single-phase $FeSb_3$ films could be prepared if a small excess of Sb is provided. These films are very smooth and no influence of the film morphology on the thermoelectric properties is expected. Furthermore, the theoretical results nicely support the extracted parameters of the crystal structure and can be used for the calculation of the electronic structure.

3. *Thermoelectric properties of* Fe-Sb *thin films*

The transport coefficients determined at room temperature are summarized in Fig. 4 for Fe-Sb films annealed in UHV at different temperatures. The composition range of single-phase skutterudite films is additionally marked in Fig. 4(f) by bars.

The electric conductivity σ of the Fe-Sb films is comparably low and reveals only a weak dependence on the Sb content [Fig. 4(a)]. Only an increase from about 1 to about 2 $(m\Omega cm)^{-1}$ is observed for a Sb content of ~75 at. %, which might be related to the formation of the single-phase $FeSb_3$ skutterudite. This low magnitude and the independence on compositional changes are an indication of a heavily doped or degenerated semiconductor showing metal-like behavior, which is also supported by the valence electron count (VEC) of 68 [36]. Only for a VEC of 72 is semiconducting behavior expected [36]. On the contrary, Möchel *et al.* [4] published temperature-dependent resistivity measurements for $FeSb_3$ prepared by MERM and obtained a semiconducting character with a band gap of 16.3 meV. However, our room-temperature conductivity is about four times larger than the value presented there.

Hall measurements deliver deeper insights and show p-type conduction. The effective charge-carrier concentration reveals large values of the order of 10^{22} cm^{-3} [Fig. 4(c)], while the effective Hall mobility is around 0.5 cm^2/Vs and thus extremely small [Fig. 4(d)]. The charge-carrier density increases slightly with increasing Sb content, but no obvious dependence of the mobility on the Sb content can be found. The high conductivity is therefore caused by the large charge-carrier concentration and the $FeSb_3$ films should reveal a metal-like temperature dependence.

The measured Seebeck coefficient is shown in Fig. 4(b). It has a positive sign and increases with increasing Sb content, especially for a Sb content larger than 75 at. %, for which single-phase skutterudite films are formed. The maximum value at room temperature is ~70 μV/K. Since the Hall constant and Seebeck coefficient both give a positive sign, hole conduction dominates in these films. However, the large Seebeck coefficients are quite surprising, since the obtained electric properties reveal rather metallic behavior than semiconducting properties, and thus a smaller Seebeck coefficient S is expected.

Using the values of the conductivity and the Seebeck coefficient, the power factor $S^2\sigma$ at room temperature was calculated giving a maximum value of about 10 $\mu W/K^2cm$ for a Sb content of 77 at. % [Fig. 4(e)]. The maximal power factor with respect to the composition is not reached in this study, since it is still increasing with increasing Sb content.

Please note that the real Seebeck coefficient of the films is assumed to be larger than the presented values, which is caused by thermal shortening of the film due to the large thermal conductivity of the Si substrate. A lot of heat is actually bypassed from the hot Cu block to the cold one

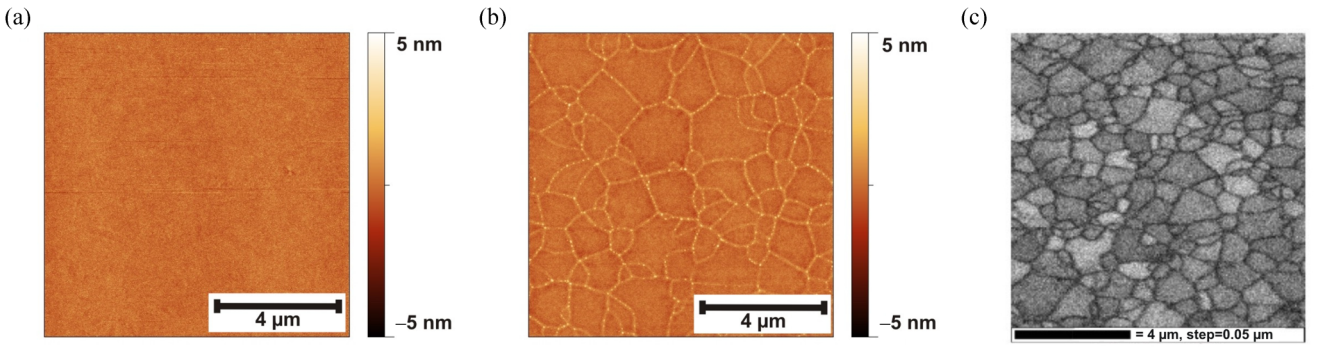

FIG. 3. (Color online) AFM image of a $FeSb_3$ film with a Sb content of 77 at. % obtained after annealing at (a) 250 and (b) 300 °C. (c) EBSD band contrast map of the film annealed at 300 °C.

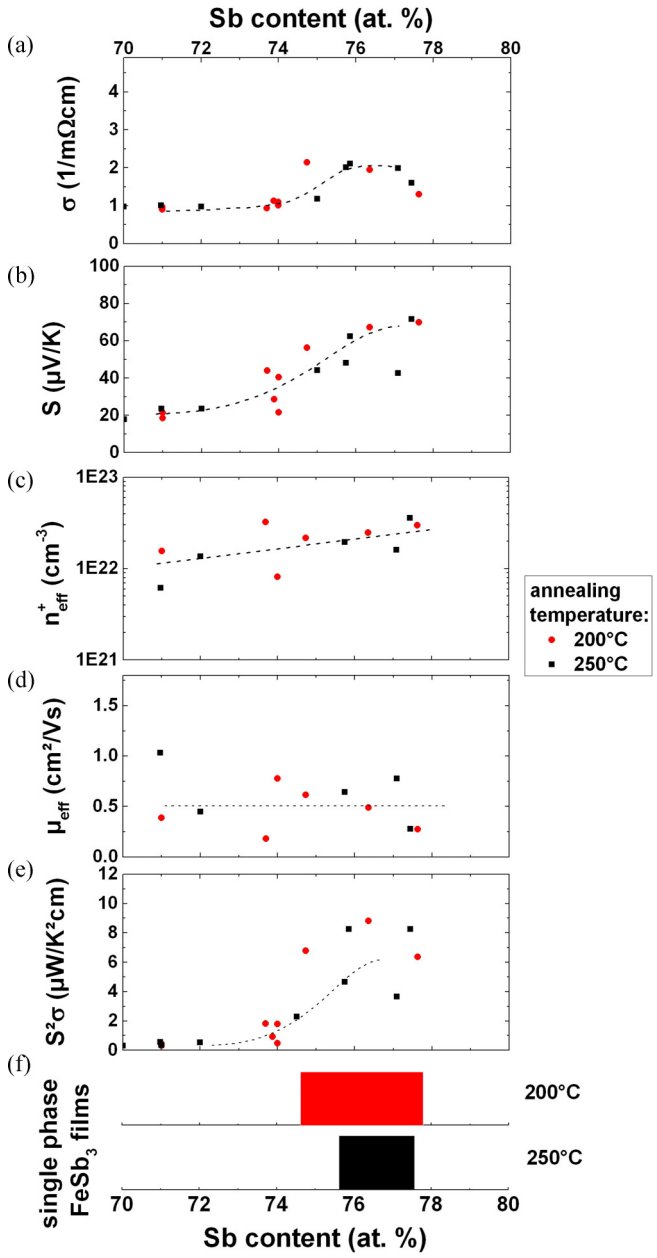

FIG. 4. (Color online) (a)–(e) Thermoelectric properties of Fe-Sb films with different Sb content at room temperature. The films were deposited at room temperature and postannealed at 200 and 250 °C. The dashed lines are a guide to the eye and the superscript "+" in the label of the effective charge-carrier density indicates *p*-type conduction (positive Hall constant). (f) The composition range of single-phase skutterudite films is marked by bars. Films with a Sb content lower than 73 at. % do not contain the skutterudite phase at all.

and thus the experimentally measured temperature gradient of the film is larger than the applied one. However, the SiO_2(100 nm)/Si(100) substrates are similar for all samples and should therefore give about the same quantitative change of the Seebeck coefficient. To estimate the change of the absolute value due to the thermal shortening and to confirm this claim, several Fe-Sb films were simultaneously prepared on the special glass substrates. The observed underestimation of the Seebeck coefficient on SiO_2(100 nm)/Si(100) at room temperature for these films was about 50% and would account for a correction of the presented power factors by a factor of 2.25. Therefore, only films prepared on these special glass substrates are used for the temperature-dependent measurements.

B. Electronic structure and computed transport properties at room temperature

The electronic structure and the corresponding intrinsic transport properties at room temperature were calculated to provide deeper insights into these contrary results for the electric conductivity and the Seebeck coefficient. The calculations are based on the relaxed structural parameters given in Table II.

All applied functionals (LDA, PBE, PW91) show qualitatively very similar results for the density of states (DOS) and the electronic band structure. An example is depicted in Fig. 5, which shows the PBE results for the optimized PBE lattice structure. The band structure and the density of states were calculated both spin polarized and unpolarized, and the computed results yield a magnetic ground state of $FeSb_3$. This is also in agreement with other theoretical studies [37]. However, magnetic measurements between 4 K and room temperature (not shown) give no indication of a ferromagnetic ground state, which is also in agreement with earlier experimental studies [4] and might be explained by different properties of thin-film samples compared to bulk (e.g., stress, impurities, surface distortions). Thus the following computed transport properties are derived solely from the unpolarized band structure.

In general, the total density of states and the band structure agree well with data obtained for a skutterudite compound [34] and the Fermi level is lying in the valence band close to the band gap, as shown in Fig. 5(a). As for $CoSb_3$, there are many bands with metallic *d*-state character close to the Fermi level and a single valence band with strong dispersion defining the gap width at the Γ point. However, the single valence band of $FeSb_3$ is in contrast to $CoSb_3$ solely of the Sb(*p*) state character and crossed by other bands. The Fermi energy, lying in the valence band, confirms a *p*-type metallic behavior, as expected from the conductivity and Hall measurements. In this sense, $FeSb_3$ can be thought of as a *p*-doped skutterudite.

The conductivity, the Seebeck coefficient, and the power factor were calculated from the electronic structure, and the achieved results are depicted in Fig. 6 with respect to the chemical potential and for a temperature of 300 K. Due to the unknown relaxation time, a direct comparison with the experiment is only possible for the Seebeck coefficient. However, the computed results allow one to derive general trends for the transport properties with respect to the chemical potential, i.e., the doping or the number of carriers.

$FeSb_3$ is *p*-type metallic for $\mu = 0$ eV and thus a comparably large conductivity [Fig. 6(a)] and only a small Seebeck coefficient [Fig. 6(b)] can be found. If the chemical potential is further decreased (*p*-type doping), the conductivity becomes strongly enhanced due to the increasing number of states at both sides of the chemical potential necessary for charge-carrier excitation, which results in a larger charge-carrier density. These states correspond mainly to the Fe *d* states,

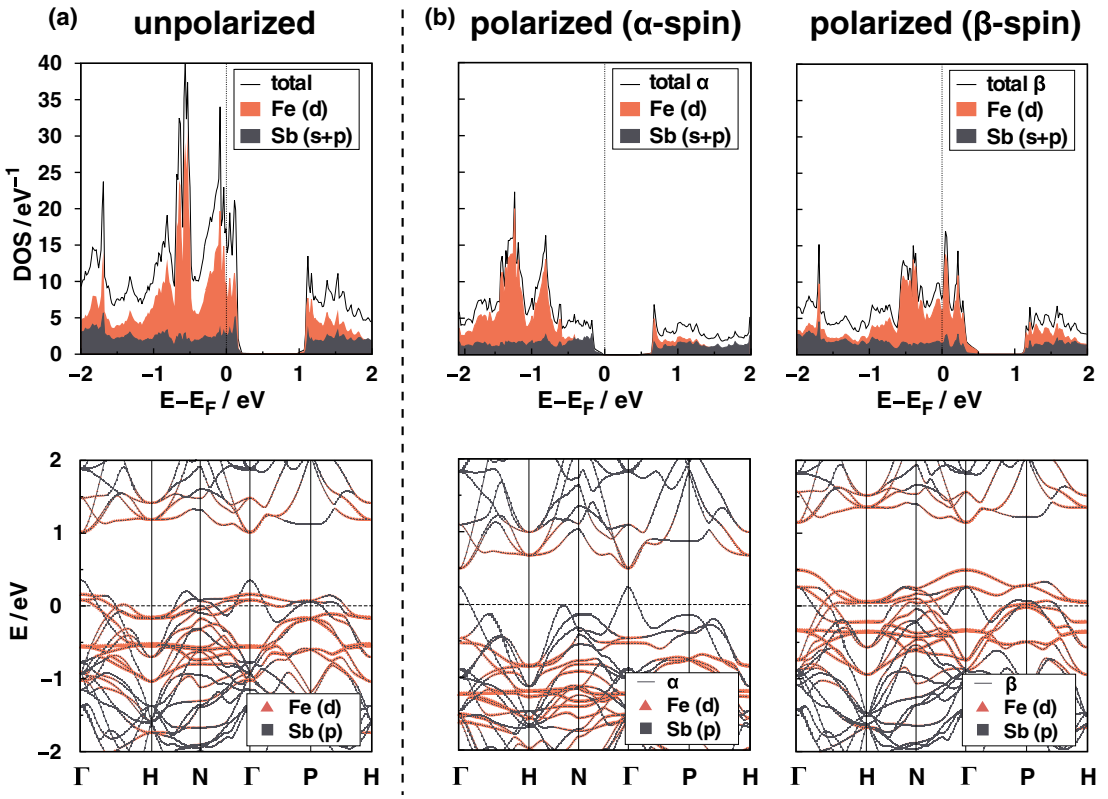

FIG. 5. (Color online) Density of states [Sb(p), Fe(d) projected, and total] and band structure of the $FeSb_3$ skutterudite structure obtained by DFT/PBE calculations: (a) unpolarized and (b) polarized. In the case of a polarized calculation, different results are achieved for different spin orientations.

as visualized by the DOS in Fig. 5(a). However, the increase in carrier density also yields a small Seebeck coefficient for p-type doping. The maximum of the conductivity is reached for a chemical potential of -0.39 eV, leading to the maximum of the power factor at -0.21 eV.

For n-type doping, for instance by an excess of Sb, the chemical potential is shifted closer to the band gap. Please note that only weak n-type doping is discussed, which should yield a slight increase of the chemical potential and not a compensation of the p-type character of $FeSb_3$ by completely shifting the chemical potential into the conducting band, resulting in n-type conduction. In this case of weak n-type doping, the conductivity decreases due to the decreasing number of states above the chemical potential. A lower number of charge carriers can be excited and the charge-carrier density decreases. In contrast, the Seebeck coefficient is strongly enhanced and becomes largest in the gap, where it is dominated by the single valence band. This can be explained, for instance,

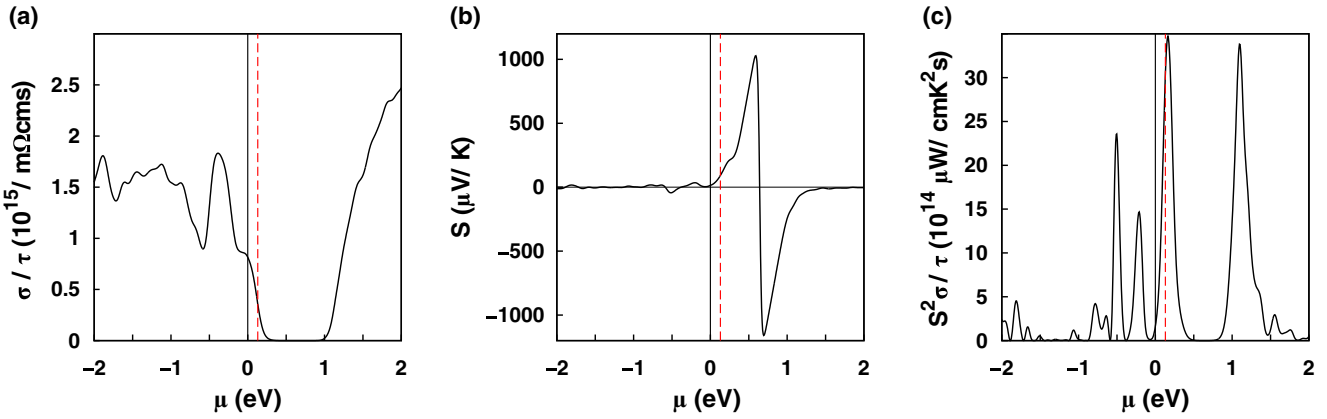

FIG. 6. (Color online) Semiclassical transport properties at 300 K as obtained by DFT/PBE and BOLTZTRAP [31] with respect to the chemical potential: (a) electric conductivity, (b) Seebeck coefficient, and (c) power factor. The solid black line indicates the calculated Fermi level. The dotted red line indicates the chemical potential that corresponds to the experimental charge-carrier density of 8×10^{21} cm^{-3} and thus to a $FeSb_3$ film with excess Sb.

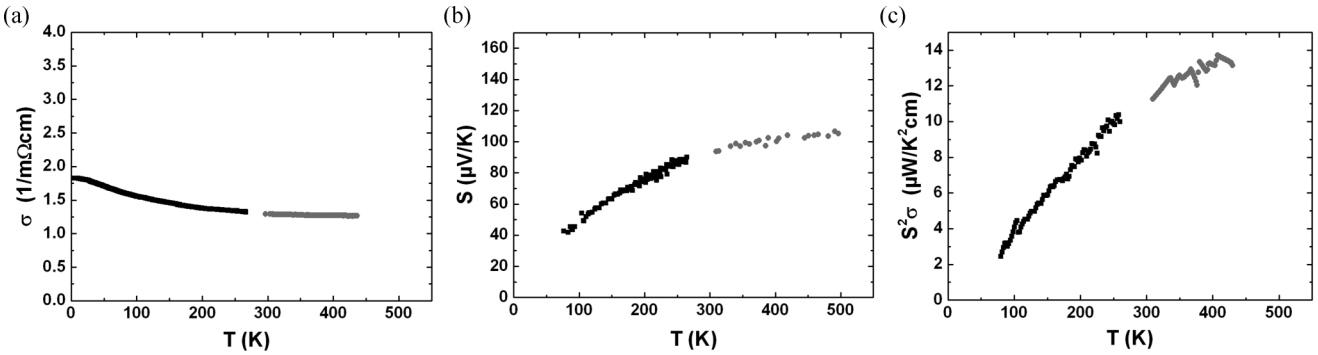

FIG. 7. Transport coefficients of a $FeSb_3$ film with a Sb content of 76 at. %: (a) electric conductivity σ, (b) Seebeck coefficient S, and (c) power factor $S^2\sigma$. The low-temperature measurements (black) are carried out in a cryostat, while the high-temperature measurements (gray) are performed in a homemade vacuum setup.

by the following equation for the Seebeck coefficient S [38]:

$$S = \frac{1}{\sigma_{\text{ges}}} \sum_{i=1}^{N} \sigma_i S_i .$$

Here, S_i and σ_i are the conductivity and the Seebeck coefficient of a single band i, and σ_{ges} is the overall conductivity. From the general Boltzmann theory follows that S_i becomes largest if the corresponding band i exhibits a large distance to the chemical potential [38]. S_i is therefore large for the single valence band if the chemical potential lies in the gap. Furthermore, from the equation, it also follows that the contribution of a specific S_i to the overall Seebeck coefficient is higher if the contribution $\sigma_i/\sigma_{\text{ges}}$ of this band i to the overall conductivity is also large. This is also fulfilled for the single valence band if the chemical potential lies in the gap or close to it, since no other bands exist in the gap, which could additionally contribute to the conduction. Thus the Seebeck coefficient increases by n-type doping and reaches its maximum for a chemical potential of $\mu = 0.59$ eV. For larger chemical potentials, the Seebeck coefficient is again lowered by the influence of the n-type conduction bands. The increase of the Seebeck coefficient also leads to a maximum of the power factor at $\mu = 0.16$ eV [Fig. 6(c)]. It is slightly shifted compared to the maximum of the Seebeck coefficient due to the decreasing conductivity.

To conclude, stoichiometric $FeSb_3$ exhibits a low power factor, which can be strongly enhanced by weak p- or n-type doping. The n-type doping results in large Seebeck coefficients, while the metallic behavior is maintained (chemical potential lies still in the band). This is in agreement with the investigated single-phase $FeSb_3$ samples and an n-type doping is indeed expected due to the excess of Sb. Details will be discussed in the following section.

C. Temperature-dependent transport coefficients of a $FeSb_3$ skutterudite thin film

Temperature-dependent transport measurements were performed for a $FeSb_3$ skutterudite thin film fabricated by codeposition at room temperature on the Ohara special glass substrate followed by postannealing in UHV at 280 °C. The Sb content of the as-deposited film was (76 ± 2) at. %. The structural investigation of the annealed film reveals a single-phase skutterudite film with a mean grain size of 1.1 μm and a smooth surface without cracks, which are avoided due to the similar expansion coefficient of the glass substrate [35].

Furthermore, the measured temperature-dependent transport properties were compared with calculations based on the unpolarized electronic band structure shown in Fig. 5(a). The calculations were performed for three different chemical potentials μ, which all correspond to a certain level of doping:

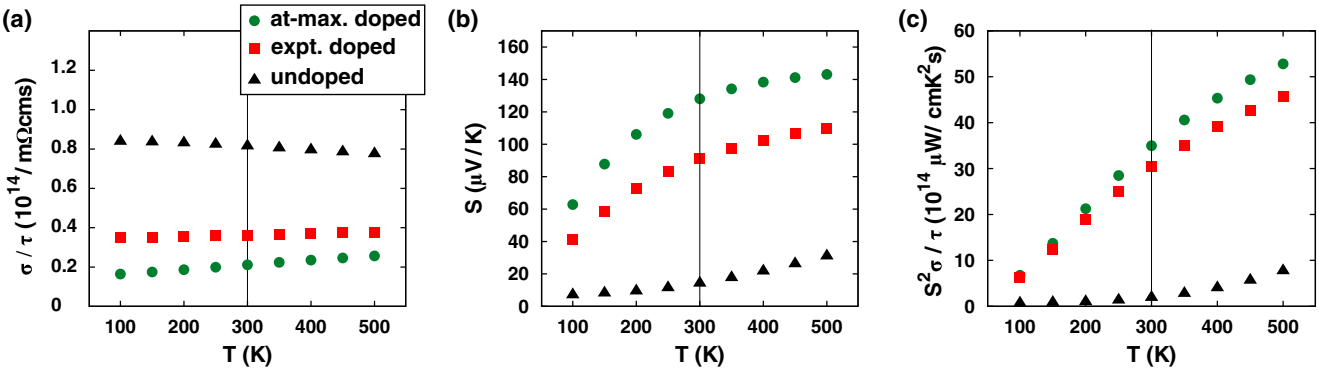

FIG. 8. (Color online) Semiclassical transport properties as obtained by DFT/PBE and BOLTZTRAP [31] with respect to the temperature T and to the selected hypothetical doping levels: (a) electric conductivity over relaxation time, (b) Seebeck coefficient, and (c) power factor over relaxation time.

$\mu = 0$ eV corresponds to no doping and considers solely the intrinsic behavior of the material, while $\mu = 0.13$ eV corresponds to the experimentally observed carrier concentration of the prepared film of 8×10^{21} cm^{-3} at room temperature, as indicated by the red dotted line in Fig. 6. Please note that this value corresponds to slight *n*-type doping, which can be explained by the excess of Sb compared to stoichiometric films [32]. In Fig. 6, it can also be seen that the determined chemical potential is close to the theoretical maximum of the power factor at room temperature of $\mu = 0.16$ eV, which was probed as the third case. In the following, we will refer to the three theoretical cases as undoped, experimentally doped, and at-maximum doped. The results of the temperature-dependent transport measurements and calculations are shown in Figs. 7 and 8, respectively. The measured conductivity [Fig. 7(a)] decreases slightly with temperature and the absolute value at room temperature is in agreement with the measured conductivities of the films prepared on SiO_2(100 nm)/Si(100) with similar composition. The small absolute change and the negative slope confirm the expected metallic-like behavior. Hall measurements have shown *p*-type conduction and a slight increase of the charge-carrier density with temperature; however, the decrease of mobility corresponding to phonon scattering dominates (both not shown).

The calculated temperature-dependent conductivity shows different results for all three theoretical doping levels, as shown in Fig. 8(a). All curves exhibit only a weak temperature dependence, whereas a change from negative (metal-like) to positive (semiconducting-like) slope is observed with increasing doping level. This might also explain the different slopes obtained in this work compared to the results reported by Möchel *et al.* [4]. The measured curve (this work) shows, especially in the low-temperature range, a larger absolute change than the calculated curve with experimental doping and also a different slope. However, only phonon scattering is taken into account for the calculations, which dominates mainly at higher temperatures, where the experimental curve also approaches a constant value. Thus the relaxation time can be approximated in this temperature regime and a value of 3×10^{-14} s was determined, which is in rough agreement with the reported value of about 1.5×10^{-14} s found for $CoSb_3$ [39]. A detailed analysis of the low-temperature range is more challenging and beyond the scope of this work.

The measured Seebeck coefficient reveals no change of sign and exhibits positive values over the entire temperature range, which confirms the *p*-type conduction. It increases steadily with temperature and at 500 K a value of about 100 μV/K is obtained [Fig. 7(b)].

For all three chemical potentials and hypothetical doping levels, the calculated Seebeck coefficients are shown in Fig. 8(b). For the experimental doped case, the quantitative agreement to the experiment is excellent, which confirms the determined chemical potential and the doping of the $FeSb_3$ thin films due to excess Sb. This doping yields a favorable shift in the chemical potential, leading to surprisingly high transport coefficients compared to the calculated intrinsic values of $FeSb_3$. The calculated results for the electric conductivity and the Seebeck coefficient in the experimentally doped case are in good agreement with the experiment, and the large Seebeck coefficient in combination with the metal-like conductivity can therefore be explained by the specific features of the electronic band structure of $FeSb_3$.

From both investigated parameters, the temperature dependence of the power factor $S^2\sigma$ can be extracted, as shown in Figs. 7(c) and 8(c). The measured power factor increases nearly linearly with temperature and reaches quite large values above room temperature. Qualitatively good agreement is again achieved when the curve of the measured power factor is compared to the theoretical one for the hypothetical experimental doping. Besides the good agreement, the theoretical power factor allows for two further conclusions to be drawn. First, doping is necessary to achieve a high power factor. Second, in our experimental setting, the doping is already very close to a theoretical optimum, leading to a maximal power factor. The possible benefit of further improvement of the doping level is less than 10%, as can be seen by comparing the calculated curves of the experimentally and the maximum doped case in Fig. 8(c). Thus, further improvement of $FeSb_3$ as a thermoelectric material has to focus on lowering the thermal conductivity (e.g., by filling or nanostructuring) or on improving the charge-carrier mobility by reducing the scattering rate of the charge carriers.

IV. SUMMARY

It was demonstrated that single-phase $FeSb_3$ films can be prepared by MBE deposition at room temperature followed by postannealing. This implies that eventually occurring preordering processes during the codeposition do not result in nucleation sites for the more stable phases such as $FeSb_2$. Single-phase $FeSb_3$ films could be prepared if a small excess of Sb is provided.

The electric conductivity of $FeSb_3$ films revealed metallic-like behavior and large hole densities are observed. However, the Seebeck coefficient exhibits surprisingly high values for single-phase skutterudite films, resulting in a promising power factor. Calculations of the electronic band structure and of the corresponding transport parameters verify that this promising combination, i.e., large Seebeck coefficient and high conductivity, is due to the specific shape of the $FeSb_3$ band structure.

ACKNOWLEDGMENTS

The authors thank the German Research Foundation (DFG) for funding this work via the priority program SPP 1386 "Nanostructured thermoelectrics." This project was further supported by the North-German Supercomputing Alliance (Norddeutscher Verbund zur Förderung des Hoch- und Höchstleistungsrechnens - HLRN) and the Zentraleinrichtung für Datenverarbeitung (ZEDAT) at the Freie Universität Berlin. We would also like to thank the Helmholtz-Zentrum Dresden-Rossendorf (Germany) for the possibility to perform RBS measurements and especially R. Willhelm for his scientific support. D.C.J. acknowledges support from the National Science Foundation under Grant No. DMR-1266217.

[1] G. A. Slack, in *CRC Handbook of Thermoelectrics*, edited by D. M. Rowe (CRC, Boca Raton, FL, 1995).

[2] G. S. Nolas, D. T. Morelli, and T. M. Tritt, Annu. Rev. Mater. Sci. **29**, 89 (1999).

[3] G. Rogl, D. Setman, E. Schafler, J. Horky, M. Kerber, M. Zehetbauer, M. Falmbigl, P. Rogl, E. Royanian, and E. Bauer, Acta Mater. **60**, 2146 (2012).

[4] A. Möchel, I. Sergueev, N. Nguyen, G. J. Long, F. Grandjean, D. C. Johnson, and R. P. Hermann, Phys. Rev. B. **84**, 064302 (2011).

[5] J. R. Williams, M. Johnson, and D. C. Johnson, J. Am. Chem. Soc **123**, 1645 (2001).

[6] M. D. Hornbostel, E. J. Hyer, J. Thiel, and D. C. Johnson, J. Am. Chem. Soc **119**, 2665 (1997).

[7] Ohara Company, http://www.ohara-gmbh.com/bn.

[8] M. V. Daniel, C. Brombacher, G. Beddies, N. Jöhrmann, M. Hietschold, D. C. Johnson, Z. Aabdin, N. Peranio, O. Eibl, and M. Albrecht, J. Alloys Comp. **624**, 216 (2015).

[9] W. A. Rachinger, J. Sci. Instrum. **25**, 254 (1948).

[10] JCPDS-International Center of Diffraction Data database, 1999.

[11] J. Rodriguez-Carvajal, Physica B **192**, 55 (1993).

[12] Computer code FULLPROF, http://www.ill.eu/sites/fullprof/index.html, Institute Laue-Langevin (ILL), 38000 Grenoble, France.

[13] E. Compans, Rev. Sci. Instrum. **60**, 2715 (1989).

[14] R. Bentley, *Handbook of Temperature Measure Volume 3, Theory and Practice of Thermoelectric Thermometry* (Springer Verlag, Singapore, 1998).

[15] G. Kresse and J. Hafner, Phys. Rev. B **47**, 558 (1993).

[16] G. Kresse and J. Hafner, Phys. Rev. B **49**, 14251 (1994).

[17] G. Kresse and J. Furthmüller, Comput. Mat. Sci. **6**, 15 (1996).

[18] G. Kresse and J. Furthmüller, Phys. Rev. B **54**, 11169 (1996).

[19] P. E. Blöchl, Phys. Rev. B **50**, 17953 (1994).

[20] G. Kresse and D. Joubert, Phys. Rev. B **59**, 1758 (1999).

[21] L. Hedin, Phys. Rev. **139**, A796 (1965).

[22] J. P. Perdew and A. Zunger, Phys. Rev. B **23**, 5048 (1981).

[23] J. P. Perdew, K. Burke, and M. Ernzerhof, Phys. Rev. Lett. **77**, 3865 (1996).

[24] J. P. Perdew, J. A. Chevary, S. H. Vosko, K. A. Jackson, M. R. Pederson, D. J. Singh, and C. Fiolhais, Phys. Rev. B **46**, 6671 (1992).

[25] J. P. Perdew, J. Chevary, S. Vosko, K. Jackson, M. Pederson, D. Singh, and C. Fiolhais, Phys. Rev. B **48**, 4978 (1993).

[26] P. Pulay, Chem. Phys. Lett. **73**, 393 (1980).

[27] P. E. Blöchl, O. Jepsen, and O. K. Andersen, Phys. Rev. B **49**, 16223 (1994).

[28] P. B. Allen, in *Quantum Theory of Real Materials*, edited by J. R. Chelikowsky and S. G. Louie (Kluwer, Boston, 1996), pp. 219–250.

[29] J. M. Ziman, *Electrons and Phonons* (Clarendon, Oxford, 2001).

[30] C. M. Hurd, *The Hall Effect in Metals and Alloys* (Plenum, New York, 1972).

[31] G. K. H. Madsen and D. J. Singh, Comput. Phys. Commun. **175**, 67 (2006).

[32] A. L. E. Smalley, S. Kim, and D. C. Johnson, Chem. Mater. **15**, 3847 (2003).

[33] P. Haas, F. Tran, and P. Blaha, Phys. Rev. B **79**, 085104 (2009).

[34] L. Hammerschmidt, S. Schlecht, and B. Paulus, Phys. Status Solidi A **210**, 131 (2013).

[35] M. Daniel, M. Friedemann, N. Jöhrmann, A. Liebig, J. Donges, M. Hietschold, G. Beddies, and M. Albrecht, Phys. Status Solidi A **210**, 140 (2013).

[36] J.-P. Fleurial, T. Caillat, and A. Borshchevsky, *Proceedings ICT '97. XVI International Conference on Thermoelectrics* (IEEE, Dresden, 1997), pp. 1–11.

[37] M. Råsander, L. Bergqvist, and A. Delin, Phys. Rev. B **91**, 014303 (2015).

[38] R. Simon, J. Appl. Phys. **33**, 1830 (1962).

[39] W. Wei, Z. Y. Wang, L. L. Wang, H. J. Liu, R. Xiong, J. Shi, H. Li, and X. F. Tang, J. Phys. D: Appl. Phys. **42**, 115403 (2009).